Journal of Materials Chemistry A

ROYAL SOCIETY OF CHEMISTRY

PAPER

View Article Online
View Journal | View Issue

Cite this: *J. Mater. Chem. A*, 2024, **12**, 15373

Microporous carbons derived from nitrogen-rich triazatruxene-based porous organic polymers for efficient cathodic supercapacitors†

Ahmed F. Saber, Shiao-Wei Kuo and Ahmed F. M. EL-Mahdy *

Received 23rd February 2024
Accepted 17th May 2024

DOI: 10.1039/d4ta01242a

rsc.li/materials-a

Lately, there has been growing interest in utilizing conjugated microporous polymers (CMPs) as favorable electrodes for storing energy. However, certain synthesized CMPs have exhibited limitations such as depressed conductivity as well as inefficient electrochemical properties, which have hindered their feasible use. In this regard, we effectively synthesized microporous carbonaceous materials *via* calcination followed by KOH activation processes for both TAT-Cz and TAT-BCz CMPs. The resulting microporous carbons showed noteworthy characteristics, including a significantly large surface area (up to 600 $m^2\ g^{-1}$), notable pore volume (reaching 0.75 $cm^3\ g^{-1}$), superb thermal stabilization and char yield (up to 791 °C and 90%), and amorphous nature. In particular, the thermal treatment of TAT-Cz CMP at 800 °C produced the TAT-Cz-800, which displayed a remarkable electrochemical capacitance of 1005 F g^{-1} at 1.0 A g^{-1} current density. This outstanding capacitance value is comparable to those of other porous carbon materials. Additionally, TAT-Cz-800 demonstrated the best coulombic efficiencies over a span of 5000 cycles at 10 A g^{-1} reaching 98.59%. Moreover, the excellent energy density for TAT-Cz-800 carbons was determined to be 139.58 W h kg^{-1} at a power density of 500 W kg^{-1}. Interestingly, a two-electrode symmetric SC holding TAT-Cz-800 displayed a superb electrochemical capacitance of 458 F g^{-1} at 1.0 A g^{-1}, and a higher energy density up to 63.61 W h kg^{-1}. The exceptional electrochemical efficacy of TAT-Cz-800 as an electrode for energy storage is likely due to its large surface area, highly porous carbon structure, and high degree of nitrogen and oxygen contents.

Introduction

The past decade has seen significant advancements and increased focus on clean and sustainable energy sources due to the growing concerns about environmental pollution, climate changes, and the need to address energy security. To combat these challenges, various countries have dedicated resources and research to the development of clean and recyclable energy technologies. Notable examples include solar energy, nuclear power, wind energy, and innovations in energy storage like supercapacitors (SCs).[1–3] Among the spectrum of energy storage technologies, SCs have garnered notable attention due to their distinctive attributes such as remarkable power density, robust cycle stability, rapid charge–discharge capabilities, and a safety profile that remains intact. Despite some drawbacks, such as lower energy density, these qualities position SCs as compelling contenders for energy storage.[4–7] There are two distinct categories of SCs, differentiated by their release mechanisms and energy storage modes: pseudocapacitors and electrochemical double-layer capacitors (EDLCs).[8]

Conjugated microporous polymers (CMPs)[9–12] represent a novel class of porous organic polymers (POPs),[13–15] distinguished by their intricate networks of nanopores and extended π-conjugation. The fabrication of CMPs has conventionally involved employing C–N or C–C coupling reactions. These reactions encompass methodologies such as Buchwald amination, cyclotrimerization, Schiff base reaction, phenazine rings fusion, Suzuki reaction, Yamamoto reaction, Sonogashira reaction, and oxidative polymerization.[16–20] The synthesized CMPs have a diverse array of applications such as energy storage and conversion, chemosensing, catalytic systems, gas separation, organic light-emitting diode (OLED) technologies, as well as biological sciences.[21–28] Due to the diversity of building blocks comprising CMP structures, their inherent structural tunability, and their capacity for modifying π-conjugated segments, CMPs offer several advantages over conventional electrode materials when using in SCs applications.[29–34] CMPs are frequently utilized in SCs, partly due to their cost-effectiveness and widespread availability, however, certain synthesized CMPs exhibited limited electrical conductivity and inadequate redox efficiency, impeding their practical applicability.

Department of Materials and Optoelectronic Science, National Sun Yat-Sen University, Kaohsiung 80424, Taiwan. E-mail: ahmedelmahdy@mail.nsysu.edu.tw

† Electronic supplementary information (ESI) available. See DOI: https://doi.org/10.1039/d4ta01242a

The fabrication of porous carbon materials has garnered considerable interest owing to their intriguing characteristics. These encompass exceptional electrical conductivity, substantial pore volumes, large surface areas, and robust stabilities.[35,36] Consequently, porous carbons have found applications across a spectrum of practical scenarios. Notable examples include their use in gas separation and capture, catalytic processes, fuel cell technologies, energy storage, water treatment, as well as shielding electromagnetic interfaces.[37–44] As stated in the literature, the synthesis of porous carbonaceous materials possessing exceptional porosity and substantial surface area can be accomplished through chemical activation techniques, applicable to numerous polymer precursors. Notable examples of these polymers encompass CMPs, metal–organic frameworks (MOFs), porous aromatic frameworks (PAFs), and hypercrosslinked polymers (HCPs).[39–41]

Porous carbons have been synthesized using a carbonization-activation approach. Typically, carbonization involves heating organic precursors within a range of 400 to 1000 °C under inert conditions. Carbonization yields nonporous solid carbons, often referred to as biochar. The introduction of pore-forming agents, also known as porogens, is employed during the activation process to generate pores. The acquired biochar subsequently engages in oxidation reactions utilizing activation agents. These agents include O_2, air, CO_2, or H_2O in physical activation, and KOH, H_3PO_4, $ZnCl_2$, or Na_2CO_3 for chemical activation.[45,46] The chemical activation approach is commonly applied to generate carbons exhibiting large surface areas ranging from 1000 to 3000 $m^2\ g^{-1}$, by the utilization of activation agents such as KOH or NaOH.[47,48] When dealing with electrode materials intended for SCs, the macropores within porous carbons function as reservoirs for electrolyte ions. In addition, mesopores function as channels for the diffusion of ions, whereas micropores have a predominant role in ion storage, as they significantly contribute to both great surface area and electrochemical capacitance, surpassing the contributions of mesopores and macropores.

For instance, Kuo *et al.* have synthesized bio-derived polybenzoxazine containing cyano group (VFBZ-CN). The thermal calcination at 700 °C and 800 °C, accompanied by KOH activation, resulted in poly(VFBZ-CN)-700 and poly(VFBZ-CN)-800 respectively, which were applied as electrodes for SCs. The highest capacitance was measured to be 506 F g^{-1} for poly(VFBZ-CN)-800 at 0.5 A g^{-1} in a KOH solution.[49] Also, the same group constructed meso/microporous carbons (TPE-CPOP1-800 and TPE-CPOP2-800) *via* these procedures and examined their electrochemical behavior. TPE-CPOP1-800 exhibited the highest capacitance of 453 F g^{-1} at 0.5 A g^{-1} with good cyclic stabilities for 10 000 cycles at 20 A g^{-1}.[50] Moreover, we have synthesized porous carbonaceous carbons through calcination and KOH activation of tetraphenylcyclopentadiene-based CMPs (CP-TCT-700 and CPM-TCT-700) and applied them as cathodic electrodes for SCs. The top capacitance was measured to be 83 F g^{-1} for CP-TCT-700 at 1.0 A g^{-1} current density.[51]

Triazatruxene, or triindole with molecular structure resembling a planar disk, adopts ordered columnar configurations through π–orbitals interaction which favors the charge carrier's migration in one-dimension.[52] This extended conjugation, in which three carbazole building blocks share one benzene ring, can readily undergoes functionalization at various locations. Indeed, the capability for symmetric functionalization at the 3, 8, and 13 sites allows for an extensive expansion of its π-core. Triazatruxene emerges as a compelling building unit for the preparation of robust organic semiconductors, showcasing potential in diverse optoelectronic applications.[53] Indeed, certain derivatives of triazatruxene have been documented as viable organic substances in the realm of OLEDs,[54,55] organic photovoltaics (OPVs),[56] and more recently, in organic thin-film transistors (OTFTs).[57]

In this study, we focused on the fabrication of microporous carbonaceous materials through the process of calcination and KOH activation at a temperature of 800 °C. These materials were derived from TAT-Cz and TAT-BCz CMPs, which were synthesized by the Suzuki polymerization of TAT-3Br in the existence of $Pd(PPh_3)_4$ catalyst with either Cz-3BO or BCz-4BO. To understand their properties, we employed a range of analytical measurements such as Fourier transform infrared (FTIR), nuclear magnetic resonance (NMR), X-ray photoelectron spectroscopy (XPS), Raman spectra, thermal gravimetric analysis (TGA), X-ray diffraction (XRD), and BET surface area analyses to characterize their chemical composition, thermal stability, crystallinity, and surface area of the derived materials. Moreover, we conducted electrochemical measurements for the resulting polymers and their corresponding carbons, TAT-Cz-800, and TAT-BCz-800, to evaluate their suitability for energy storage applications.

Results and discussion

The significant surface area of some polymers renders them promising candidates for enhancing the efficiency of SC electrodes. Unfortunately, many reported polymers exhibit weak electrical conductivity which can indeed hinder their successful application. The addition of some conductive materials can enhance conductivity, but it inevitably leads to a decline in surface area. Recently, converting polymeric materials into their corresponding carbonaceous materials was proved to effectively resolve conductivity issues. This transformation significantly enhances their electrical mobility while maintaining the fundamental polymeric structure, resulting in electrodes with reasonably high capacitances for SCs.[58] Undoubtedly, the extent to which the electrode material in EDLCs may be reached by electrolyte ions is of utmost importance in determining the effectiveness of SCs. Therefore, porous carbons are commonly utilized as electrode components because of their large specific surface area, remarkable thermo-chemical reliability, tunable pore structure, exceptional mechanical characteristics, and high electrical conductivity.[59,60] To summarize, an ideal polymer electrode for energy storage should feature a large specific surface area, high wettability, and excellent conductivity, and hence we have chosen to use porous carbon materials as electrodes for storing energy instead of their polymer counterparts. Therefore, we chose tribromotriazatruxene (TAT-3Br) as the

starting material to facilitate Suzuki coupling polymerization with 3,6-bis(4,4,5,5-tetramethyl-1,3,2-dioxaborolan-2-yl)-9-(4-(4,4,5,5-tetramethyl-1,3,2 dioxaborolan-2-yl)phenyl)-9*H*-carbazole (Cz-3BO) and 3,3′,6,6′-tetraboronic-pinacolate-9,9′-bicarbazole (BCz-4BO), resulting in the TAT-Cz and TAT-BCz CMPs, respectively (Scheme 1). The precursors Cz-3BO, BCz-4BO, and TAT-3Br were successfully synthesized with high yields following established methods in the literature,[61–63] as outlined in the corresponding synthetic routes presented in (Schemes S1–S3†). FTIR and NMR spectra analyses were employed to confirm the effective synthesis of all utilized monomers (Fig. S1–S9†). The CMPs featuring the triazatruxene building block were synthesized through a straightforward Suzuki polymerization reaction, in which TAT-3Br was reacted with both Cz-3BO and BCz-4BO. This reaction was conducted in a co-solvent mixture of DMF and H_2O at 140 °C for 3 days, using $Pd(PPh_3)_4$ catalyst in the reaction medium (Schemes S4 and S5†). Finally, the TAT-Cz-800 and TAT-BCz-800 microporous carbons were obtained through the calcination and KOH activation of their corresponding CMPs at 800 °C under nitrogen atmosphere. The reaction yields of the as-synthesized conjugated polymers were 75.60% for TAT-Cz and 81.35% for TAT-BCz. Also, the calculated carbonization yields for the produced carbonaceous materials were 72.25% and 68.13% for TAT-Cz-800 and TAT-BCz-800, respectively. The isolated CMPs exhibited very low solubility in water and various organic solvents, indicating a high degree of crosslinking and polymerization. The FTIR and solid-state ^{13}C NMR techniques have been utilized to evaluate the perfect polymerization of monomers into polymers as well as the polymeric composition. The complete absence of B–O and C–H stretching vibrations peaks in the FTIR profile of TAT-CMPs, in comparison to its precursor Cz-3BO (1350, 2981, and 2928 cm^{-1}) and BCz-4BO (1350, 2977, and 2930 cm^{-1}), along with the disappearance of the C–Br absorption peak at 795 cm^{-1} in the TAT-3Br master monomer, demonstrates the effective C–C bond formation between the monomers, resulting in the desired polymers (Fig. S10 and S11†). Furthermore, the FTIR spectroscopy of TAT-Cz CMP revealed characteristic peaks related to C=C, C–H aliphatic, and C–H aromatic absorption bands at 1604, 2927, 2970 and 3053 cm^{-1}, respectively. In addition, the FTIR spectra of TAT-BCz CMP showed peaks at 1576, 2927, 2969 and 3052 cm^{-1} for the same stretching bonds, indicating the successful formation of the conjugated polymers with slight shifts in these vibrational frequencies compared to the starting monomers (Fig. 1A).

Additionally, the chemical structure of our polymers under study was emphasized by solid state ^{13}C NMR spectroscopy. This analysis displayed wide peaks in the range 64.93–81.71 ppm for TAT-Cz CMP and 73.83–89.83 ppm for TAT-BCz CMP, attributed to aliphatic carbons of TAT monomer. Furthermore, there are broad bands assigned to the aromatic carbons in the polymeric structures which were located in the range of 114.91–146.33 ppm for TAT-Cz polymer and 117.88–147.51 ppm for TAT-BCz polymer (Fig. 1B).

The synthesized CMPs as well as their corresponding carbonaceous materials exhibited a notable degree of stiffness and rigidity, as evidenced by their limited solubility in various solvents. TGA has been utilized to investigate the thermal

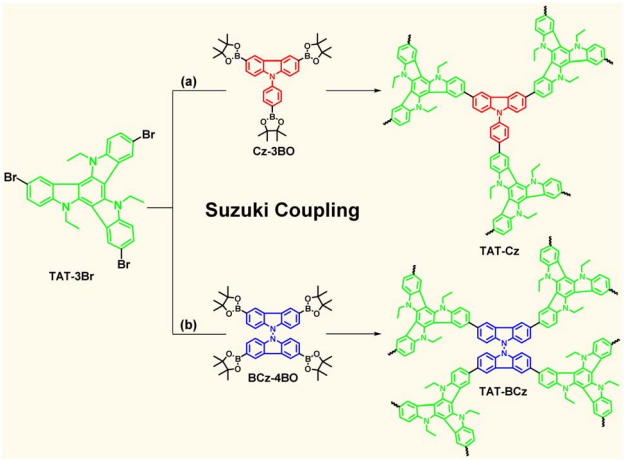

Scheme 1 Synthetic procedures of (a) TAT-Cz and (b) TAT-BCz CMPs.

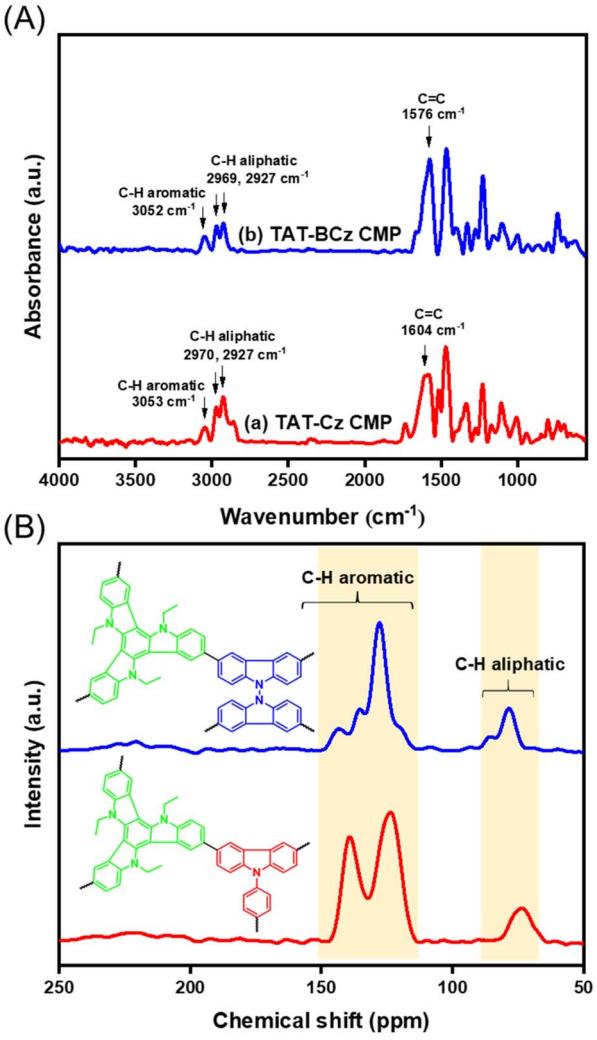

Fig. 1 (A) FTIR analyses; and (B) solid state ^{13}C NMR spectra of TAT-Cz, and TAT-BCz CMPs.

properties of polymers and carbon materials in a specific range of temperature (40 to 800 °C) under a stream N_2 gas. The TGA profiles obtained, as represented in Fig. S12,† indicated that whole studied materials, both prior and next carbonization, exhibited significant thermal stability. Specifically, TAT-Cz CMP, TAT-BCz CMP, TAT-Cz-800, and TAT-BCz-800 had 10% weight loss degradation temperatures (T_{d10}) of 536 °C, 521 °C, 791 °C, and 545 °C, respectively. In conclusion, the study also included an assessment of char yields, with TAT-Cz CMP showing an 81% yield, TAT-BCz CMP with a 76% yield, TAT-BCz-800 yielding 79%, and the highest char yield of 90% was observed for TAT-Cz-800 (Table S1†).

Fig. S13† represents the results of XPS tests conducted on the prepared microporous carbons. It contains elements including C, N and O, indicating the successful doping of nitrogen, as well as oxygen atoms into the porous carbon substrate. The TAT-Cz-800 microporous carbons displayed three prominent XPS signals: the C 1s signal at 282.81 eV, the N 1s signal at 377.47 eV, and the O 1s signal at 530.32 eV.

In addition, TAT-BCz-800 exhibited distinct peaks in the XPS spectrum, including the C 1s signal at 283.54 eV, the N 1s signal at 377.47 eV, and the O 1s signal at 531.87 eV. To examine the composition of carbon atoms in our carbonaceous materials, fitting analyses have been utilized, in which the C 1s signal of TAT-Cz-800 revealed three distinct peaks located at 283.96 eV, 284.72 eV, and 285.65 eV, characteristic of C=C, C=N, and C=O, respectively, whereas the corresponding C 1s fitting peaks for TAT-BCz-800 were centered at 283.98 eV, 284.87 eV, and 285.42 eV, respectively.[51] (Fig. 2a and d) Furthermore, fitting of the N 1s peak of TAT-Cz-800, revealing four peaks at 376.53 eV, 377.63 eV, 378.86 eV, and 380.05 eV, which were assigned to pyridinic nitrogen, pyrrolic nitrogen, quaternary nitrogen, and oxidized nitrogen functionalities, respectively.[64] The corresponding N 1s fitting values were 375.75 eV, 377.31 eV, 378.29 eV, and 379.21 eV, respectively, for TAT-BCz-800 (Fig. 2b and e). Additionally, doing fitting analysis for the O 1s signal resulted in three featured values characteristics for quinone oxygen, ether oxygen, and carboxylic oxygen functional groups.[65] In case of TAT-Cz-800 carbons, these values were analyzed to be 530.86 eV, 531.47 eV, and 532.38 eV, respectively, whereas for TAT-BCz-800 carbon material, the corresponding values were fitted to be 530.65 eV, 531.35 eV, and 532.89 eV, respectively (Fig. 2c and f).

The XPS data were summarized in Table S2.† As expected, both TAT-Cz-800 and TAT-BCz-800 carbons had higher carbon content, accounting for 80.23% and 83.57%, respectively. However, owing to nitrogen and oxygen doping, the carbon percentage of TAT-Cz-800 is relatively decreased, and the introduced nitrogen content was 11.06% for TAT-Cz-800 compared to 8.45% for TAT-BCz-800. It can also be observed that the relative oxygen content increased slightly, from 7.98% for TAT-BCz-800 to 8.71% for TAT-Cz-800. Heteroatom doping of microporous carbons can enhance hydrophilicity, stability, specific capacitance, and electrochemical efficiency as well.[66]

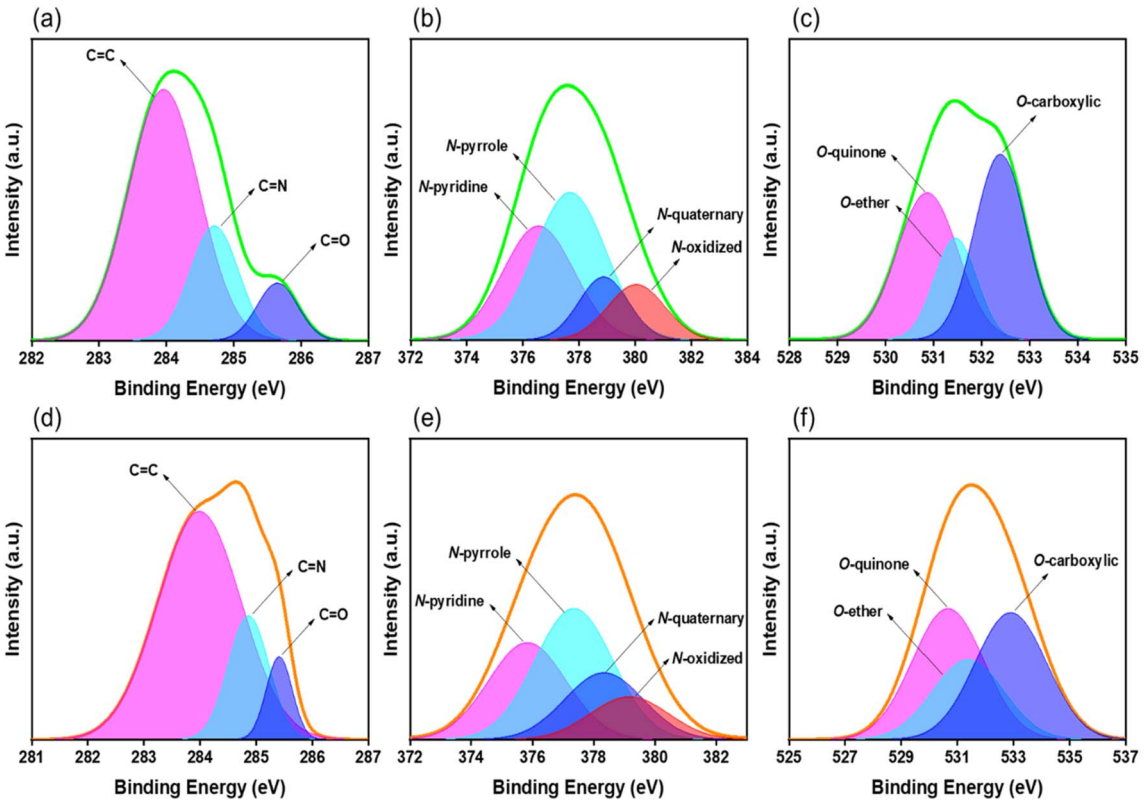

Fig. 2 XPS analyses of (a) C 1s peak, (b) N 1s peak, and (c) O 1s peak of TAT-Cz-800; (d) C 1s peak, (e) N 1s peak, and (f) O 1s peak of TAT-BCz-800.

From Table S3,† the doping nitrogen of TAT-Cz-800 was composed of 32.5%, 42.2% 12.6%, and 12.7% attributed to N-pyridinic, N-pyrrolic, N-quaternary, and N-oxidized, respectively. The corresponding values for TAT-BCz-800 were 28.7%, 38.9%, 19.8%, and 12.6%, respectively. N-Quaternary compounds have the ability to enhance redox processes, as well as boost the rate of electronic transfer and conductivity.[67–69] N-Pyridinic and N-pyrrolic functionalities can enhance electrochemical performance by providing abundantly accessible defects, thus facilitating sufficient energy storage and active centers.[70] They also contribute significantly to pseudocapacitance, thereby making a substantial contribution to electrochemical capacities.[71,72] The oxygen content of TAT-Cz-800 mainly consisted of 39.3%, 18.7%, and 42.0% which related to O-quinone, O-ether, and O-carboxylic, respectively, whereas the TAT-BCz-800 exhibited the corresponding values as 38.8%, 23.6%, and 37.6%, respectively. The presence of pseudocapacitance from the oxygen-containing functionalities is dependent on a reversible faradaic redox mechanism.[73,74] Acidic functionalities, particularly carboxyl groups, undergo reactions with hydroxyl ions in alkaline solutions, leading to improved electrochemical efficiency.[75,76] Consequently, the TAT-Cz-800 with higher nitrogen and oxygen contents had greater electrochemical capacitance and power density than the TAT-BCz-800 counterpart.

Besides that, XPS was effectively determined the chemical bonding characteristics as well as the carbon and nitrogen contents of the starting TAT-Cz and TAT-BCz polymers. The XPS survey spectrum revealed two prominent signals: C 1s signal at 285.67 eV for the TAT-Cz and TAT-BCz CMPs, in addition to N 1s signals at 401.09 eV and 400.64 eV, for the TAT-Cz and TAT-BCz CMPs respectively (Fig. S14†).

As shown in (Fig. S15a and c†), two peaks were observed in the high-resolution spectrum of the C 1s signal which was mainly assigned to C=C (284.05 eV for TAT-Cz CMP and 284.02 eV for TAT-BCz CMP) and C–N (284.79 eV for TAT-Cz CMP and 284.93 eV for TAT-BCz CMP). In addition, the N 1s spectrum of the TAT-Cz polymer has been fitted for only one peak at 399.63 eV characteristic of C–N, whereas for TAT-BCz CMP, it had a broad peak at 399.57 eV which was attributed to C–N and N–N functional groups. (Fig. S15b and d†) The elemental compositions and percentage of every functionality were given in Tables S2–S4.†

By comparing the XPS results before and after calcination and KOH activation processes, one can conclude that there is a perfect conversion of polymers into their corresponding doped carbons with varying compositions. There is no oxygen content in the original polymers, but high carbon content and oxygen-doping appeared in the produced carbon materials. These results have exactly resembled those of reported carbon materials[49,51,77] with definite chemical structure as represented in (Fig. S16†).

The XRD patterns revealed the presence of three sharp diffraction peaks at 2θ of 21.31°, 29.76°, and 30.78°, assigned to the graphitic stacking of the (002) and (100) planes.[77] Furthermore, a notable XRD peak at a value of 43.42°, corresponding to the (101) plane, confirmed the existence of a graphitic structure.[78] These results underscore the successful conversion of the polymeric precursors into their corresponding carbon materials. As a result, both TAT-Cz-800 and TAT-BCz-800 exhibited irregular and amorphous carbon structures, contributing to substantial porosity, large surface area and outstanding energy storage capacity[79] (Fig. 3a).

Raman spectroscopy has been utilized to extra investigate the structural nature of the as-synthesized carbonaceous materials. The Raman spectra of TAT-Cz-800 revealed two prominent bands: the D band at 1323 cm^{-1}, signifying a defected carbon structure, and the G band at 1579 cm^{-1}, linked to the symmetry and crystallization of carbon materials. Moreover, the D and G Raman signals for TAT-BCz-800 were detected at 1329 and 1581 cm^{-1}, respectively.[80,81] Remarkably, the G-band position in TAT-BCz-800 closely resembled that of graphene (1581 cm^{-1}), signifying a more graphenoid structure compared to TAT-Cz-800. The D band to the G band intensity ratio (I_D/I_G) provides insights into carbon graphitization degree.[80] The calculations showed I_D/I_G intensity ratios of 1.20 for TAT-Cz-800

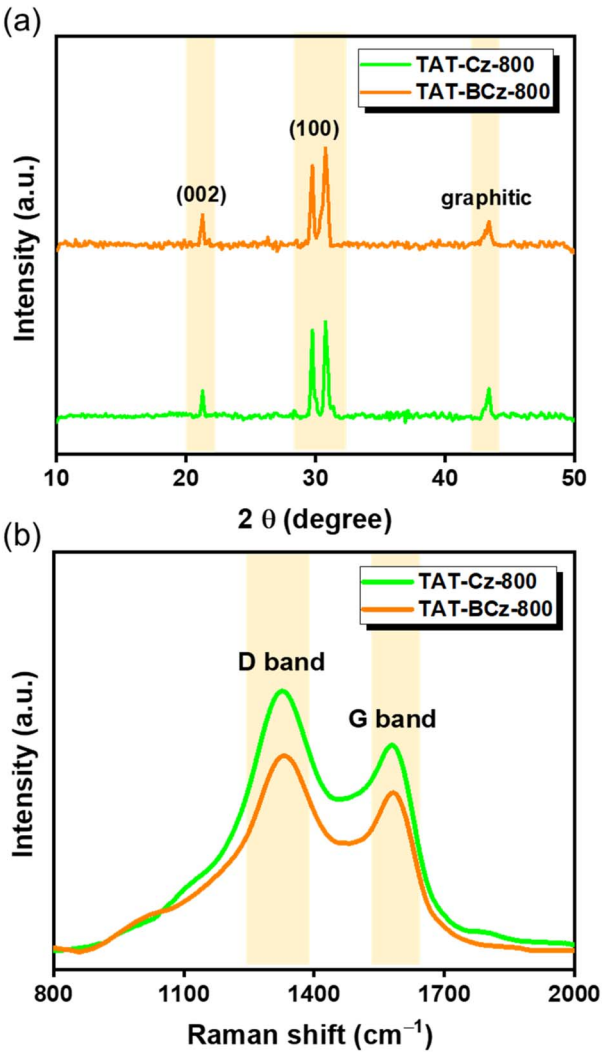

Fig. 3 (a) XRD analysis and (b) Raman spectra of TAT-Cz-800 and TAT-BCz-800.

and 1.26 for TAT-BCz-800, indicating that TAT-BCz-800 had a greater graphitization degree and a more ordered carbon structure compared to TAT-Cz-800 (Fig. 3b).[82]

Again, the successful transformation of the utilized conjugated polymers into their corresponding microporous carbons has been confirmed by comparing the XRD and Raman analyses of the polymers before and after carbonization process. XRD analysis of both TAT-Cz, and TAT-BCz CMPs revealed no diffraction peaks, demonstrating the polymers' amorphous nature in contrast to the sharp diffraction signals of their resulting carbons. (Fig. S17†) In addition, Raman profiles of the polymers exhibited faint and shifted G and D bands in comparable to those of their carbonaceous materials (Fig. S18†).

Elemental analysis has been utilized to elucidate the chemical composition of the as-synthesized polymers and their produced carbons. The results demonstrated that both TAT-Cz-800 and TAT-BCz-800 carbons are rich in carbon content with enough doped nitrogen and oxygen heteroatoms. The carbon content of TAT-BCz-800 had a value of 86.36% which is slightly higher than that of TAT-Cz-800 (78.18%). On the other hand, the TAT-Cz-800 was richer in both nitrogen and oxygen functionalities (13.22% and 8.60%, respectively) compared to those values of TAT-BCz-800 (8.29% and 5.35%, respectively). The obtained data were in full agreement with the XPS analysis, proposed chemical structure, and the electrochemical performance of the prepared porous carbon materials (Table S5†).

Generally, carbonization of COFs typically leads to the collapse of the pore architecture, which in turn causes a decline in the specific area of the surface. In contrast, CMPs that have strong covalent C–C bonds are able to preserve the integrity of these bonds even at high temperatures, which helps to prevent the pore structure from collapsing.[83] Chemical activation can enhance the specific surface area and provide ordered pore size distribution of carbonaceous materials, thereby mitigating the reduction in the specific surface area caused by pore collapse to some extent.[84–86] Furthermore, the activation on carbon materials leads to an increase in oxygen-containing functional groups which significantly enhances electrochemical efficiency.[87] Consequently, we have used this strategy of carbonization and KOH activation to improve the electrochemical efficiency of our polymers. To determine the porosity parameters of the triazatruxene-based CMPs and their corresponding carbons, low-temperature N_2 sorption isotherms have been measured. The microporosity characteristics for the as-synthesized polymers and the carbonaceous materials were confirmed and presented in (Fig. 4a and b) which follow the type-II isothermal profile. At lower relative pressure, there is a decline of N_2 uptake within the porous structure. However, a significant increase in N_2 uptake has been noticed as the relative pressure increased to be greater than 0.95 indicating the existence of additional macropores alongside the primary micropores. This phenomenon may be assigned to the interparticulate cavities resulting from the loose packing of tiny particles. The hierarchical structures and the high degree of microporosity were also proved by the hysteresis loop observed in the figures. The obtained BET surface area of TAT-Cz polymer was 485 $m^2 g^{-1}$, whereas the TAT-Cz-800 carbonaceous material

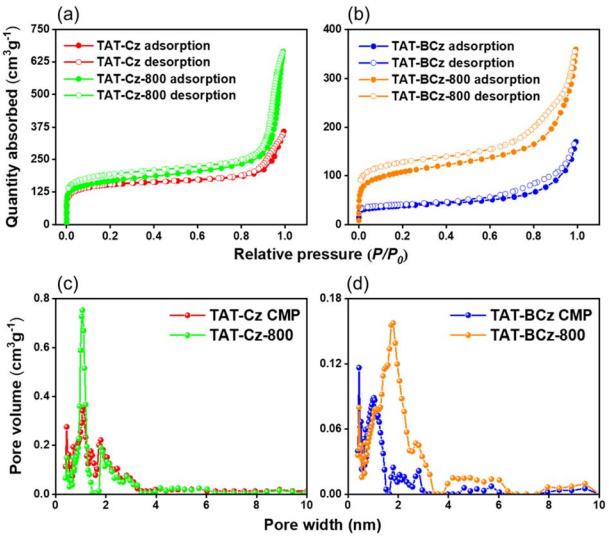

Fig. 4 Nitrogen sorption isotherms of (a) TAT-Cz CMP and TAT-Cz-800; (b) TAT-BCz CMP and TAT-BCz-800. The pore size distribution curves of (c) TAT-Cz CMP and TAT-Cz-800; (d) TAT-BCz CMP and TAT-BCz-800.

exhibited a higher BET surface area value, reaching 600 $m^2 g^{-1}$. The same behavior was observed for the second couple, in which the TAT-BCz polymer before carbonization had a lower surface area value (128 $m^2 g^{-1}$) in comparable to the corresponding carbon materials obtained after calcination (384 $m^2 g^{-1}$). Therefore, both TAT-Cz and TAT-BCz polymers with the smallest BET surface areas were suggested to have a lower electrochemical efficiency than their corresponding carbon materials. The observed pore sizes were centered at 0.96 nm for TAT-Cz CMP, 1.07 nm for TAT-Cz-800, 1.03 nm for TAT-BCz CMP and 1.80 nm for TAT-BCz-800. Moreover, The calculated pore volumes were 0.36, 0.75, 0.09 and 0.16 $cm^3 g^{-1}$ corresponding to TAT-Cz CMP, TAT-Cz-800, TAT-BCz CMP and TAT-BCz-800, respectively, indicating the existence of interfacial micropores on the surface of our electrode materials (Fig. 4c, d and Table S6†).

The morphological characteristics of both the triazatruxene-based polymers and their carbonized counterparts were investigated through scanning electron microscope (SEM) and transmission electron microscope (TEM). SEM analysis of TAT-Cz and TAT-BCz CMPs revealed the accumulation of particles of varying sizes, creating porous structures with numerous cavities. Moreover, TAT-Cz-800 and TAT-BCz-800 exhibited a flower-like morphology characterized by micro-sized cavities. The random aggregation of nanoparticles in these materials led to the formation of larger pores, which are well-suited for facilitating the ions diffusion within the electrode material (Fig. 5a–d). The polymers' external morphology was analyzed using TEM. All the CMPs and the produced carbons exhibited aggregated particles with diverse shapes (Fig. 5e–h). The low-magnification HR-TEM photos confirmed the highly uniform and microporous structure for both TAT-Cz-800 and TAT-BCz-800 carbon materials. Their pore diameters were found to be smaller than 2.0 nm. (Fig. S19†) This hierarchical and porous

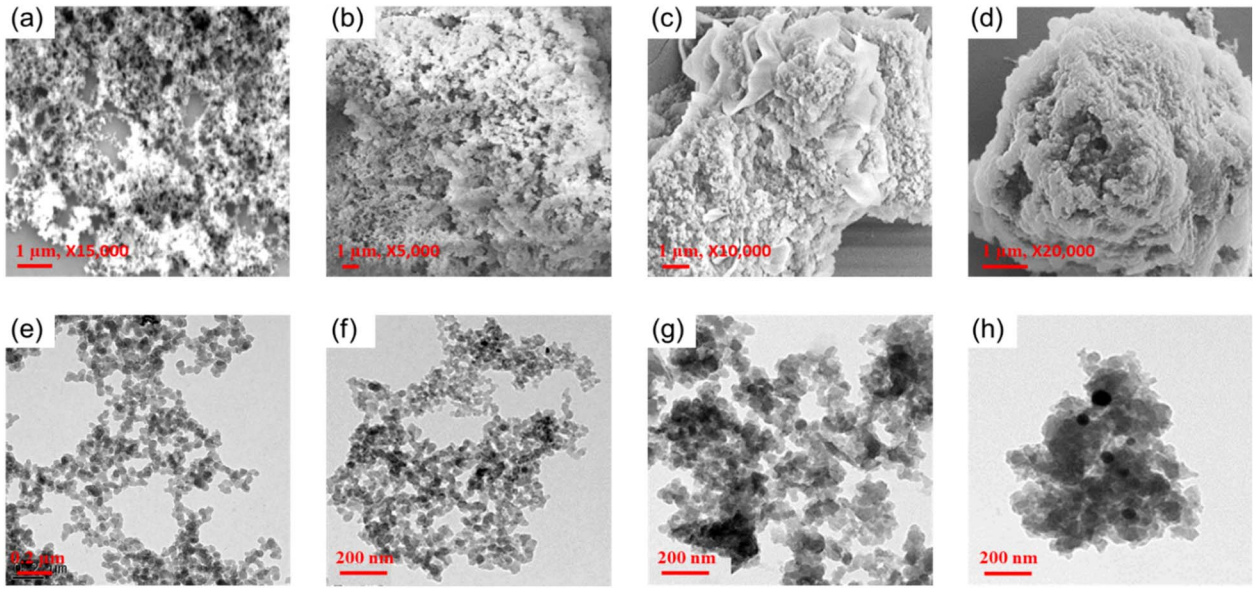

Fig. 5 SEM photos of (a) TAT-Cz CMP, (b) TAT-BCz CMP, (c) TAT-Cz-800, and (d) TAT-BCz-800. TEM photos of (e) TAT-Cz CMP, (f) TAT-BCz CMP, (g) TAT-Cz-800, and (h) TAT-BCz-800.

nature is beneficial in accelerating ion transfer, thereby enhancing the rate capacity of SCs.[65]

The electrochemical characteristics of the developed conjugated polymers and their carbonaceous materials were assessed through a three-electrode technique, involving cyclic voltammetry (CV) and galvanostatic charge–discharge (GCD) methods, in a 1 M KOH alkaline electrolyte. A comparison of the produced CV and GCD plots for both TAT-Cz and TAT-BCz polymers with those of TAT-Cz-800 and TAT-BCz-800 carbons has been studied. These CV analyses were performed over a potential window of −1.0 to 0.0 V against the Hg/HgO reference electrode, with varying sweep rates (5 mV s^{-1} to 200 mV s^{-1}) (Fig. 6a, b and 8a, b). The materials being investigated represented CV profiles with a nearly rectangular shape, occasionally accompanied by minor humps specially for the synthesized CMPs. These CV curves remained fairly consistent by raising the potentials from 5 to 200 mV s^{-1}, affirming their stabilization, and indicating the EDLC nature of their capacitance. The appearance of such small humps in the CV profiles is indeed indicative of pseudocapacitance, which can be referred to the heteroatoms content and electron-rich phenyl groups within the materials' frameworks. This phenomenon of induced pseudocapacitance enhances reversibility of redox reactions during the charge and discharge procedures.[88]

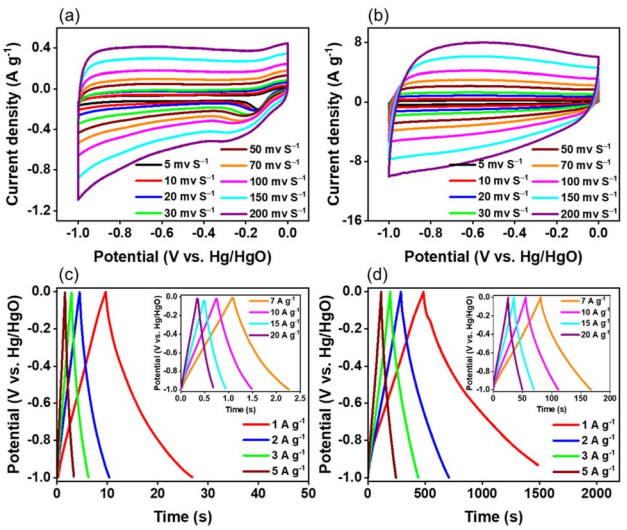

Fig. 6 CV profiles of (a) TAT-Cz CMP, and (b) TAT-Cz-800. The corresponding GCD profiles of (c) TAT-Cz CMP, and (d) TAT-Cz-800, recorded at various current densities in the three electrodes system.

The intrinsic specific surface areas as well as the existence of numerous electron-enriched phenyl rings in the as-prepared CMPs and their corresponding carbon materials contributed to the excellent coherence of their CV curves across different scan rates. Carbon materials doped with heteroatoms (*i.e.* oxygen and nitrogen), serves to boost not only their electrochemical performance but also their stability, morphology, and hydrophilicity through the introduction of various functionalities linked to their surfaces.[80] Consequently, the existence of heteroatoms, combined with unique morphologies, played a vital role in generating significant pseudocapacitance. Additionally, the improved mobility of phenyl electrons contributed to superior contact with the KOH electrolyte, ultimately leading to increased electrochemical performance. Moreover, as the sweep rate potential rises, a noticeable rise in current density is observed, and the CV curves maintain their rectangular shapes without distortion. This observation suggests great rate capability and facile kinetics.[89]

In addition, the GCD analyses were performed on the studied CMPs and their carbons at various current densities, spanning from 1.0 to 20 A g^{-1} (Fig. 6c, d and 8c, d). The obtained GCD curves exhibited triangular shapes with

inconsiderable curvature, which further supports the presence of both pseudocapacitance and EDLC mechanisms for storing energy. These observations are likely attributed to the presence of heteroatoms.[90]

The microporous carbons demonstrated prolonged GCD discharge periods in comparison to their respective triazatruxene-based polymers, signifying an enhancement in the GCD capacitance after the calcination and activation processes. These results strongly suggest that the carbonization and activation strategy promote electrochemical efficacy devoid of compromising the fundamental EDLC of the carbons.[91] Moreover, the surface area of the electrode material in EDLCs is critical as it allows for the penetration of KOH ions, significantly contributing to the improvement of SC performance. Hence, microporous carbons are a preferred choice for SC electrodes due to their exceptional properties, such as large surface area, excellent conductivity, and great thermo-chemical stability.[92]

N-Doping can enhance the asymmetric valence charge, spin density, and electron transfer ability of carbon materials. In addition, the N-pyridinic and N-pyrrolic located at the edges of nano-carbons can provide additional pseudocapacitance through the protonation/deprotonation reaction.[93] Additionally, the incorporation of oxygen-containing functional groups with strong electronegativity of oxygen atoms augments the active positions on the carbon materials, expediting charge transfer and promoting interaction between the carbons and electrolyte ions. This enhances wettability and pseudocapacitance.[94] Also, deprotonation from oxygen-bearing functionalities significantly contributes to improved wettability.[95] In addition, the insertion of oxygen-containing functionalities increases the roughness of the carbonaceous materials, which is crucial for improving hydrophilicity and wettability.[96] Moreover, the wettability of carbon electrodes is determined by the polarity of the oxygen-containing functionalities. The inherent non-polarity of carbon electrodes poses challenges for complete infiltration into polar solutions.[97]

The wettability of electrodes based on carbon materials plays a crucial role in the performance of SCs utilizing inorganic electrolytes.[98] Enhancing the wettability of carbons facilitates ion transfer, improves charge transfer, and diminishes internal resistance. This enables electrodes to attain great capacity, and prolonged cycle lifetimes.[99] Studies have indicated that the presence of oxygen-rich groups can improve the ability of carbon-based materials to be wetted by liquids.[100,101] When contact angles are small (below 90°), the liquid spreads effectively on the solid surface, suggesting relatively high wettability.[102] Hydrophobic and hydrophilic functional groups carry oxygen. Highly polarized oxygen atoms that reside in hydrophilic clusters interact with hydrogen atoms in water molecules *via* dipolar forces, improving wettability.[103]

Moreover, the oxygen-containing advantages of carbon electrodes increase their adsorption ability for various substances, preventing electrode materials from dissolving into the electrolyte promoting an uninterrupted connection within the two materials throughout long-term cycling, and facilitating high stability.[104]

In summary, an optimal electrode material for SCs should exhibit several key attributes, including a substantial surface area, excellent conductivity, fast ion transfer, and effective hydrophilicity. Consequently, carbon-based materials have become the preferred choice for SC electrodes, surpassing organic polymers, as they fulfill these critical requirements. The capacitances of the as-synthesized CMPs and the produced carbons were determined using calculations based on their GCD curves. The determined GCD capacitances for TAT-Cz CMP, TAT-Cz-800, TAT-BCz CMP, and TAT-BCz-800 were 17, 1005, 20, and 907 F g^{-1}, respectively, at 1.0 A g^{-1} (Fig. 7a and 9a). Water contact angle investigations were conducted to compare the hydrophilic behavior of the as-prepared polymers and their corresponding carbon materials. (Fig. S20†) The contact angles of TAT-Cz CMP, TAT-BCz CMP, TAT-BCz-800, and TAT-Cz-800 have been measured to be 70.1°, 54.0°, 33.1°, and 20.6°, respectively, confirming increased hydrophilicities for all materials especially the carbon materials due to their higher heteroatoms-doping. The TAT-Cz-800 with the highest nitrogen content and oxygen-containing functional groups had the maximum hydrophilicity at all which has been translated into the highest wettability to give the greatest electrochemical performance.[102] The higher capacitance of TAT-Cz-800 can be assigned to various reasons. To begin with, the higher nitrogen content in TAT-Cz-800 significantly enhances charge transportation throughout its structure. Also, the higher oxygen-containing functional groups contribute to this effect by increasing the wettability. Furthermore, the superior specific capacitance of TAT-Cz-800 across the whole current densities range, can be ascribed to its high porosity, great BET surface area, and accessible morphology. These integrated factors collectively contribute to its superior electrochemical efficacy compared to TAT-BCz-800. Therefore, the existence of higher degree of heteroatoms within the polymer framework, along

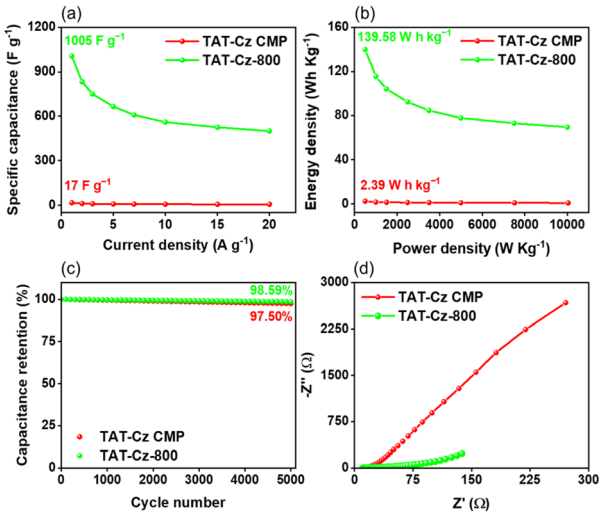

Fig. 7 (a) GCD specific capacitances of TAT-Cz CMP and TAT-Cz-800 recorded at current densities from 1.0 to 20 A g^{-1}. (b) Ragone plots. (c) Cycling retention of the electrodes, recorded at a current density of 10 A g^{-1} over 5000 cycles. (d) Nyquist plots of cells holding the as-synthesized materials in the three electrodes system.

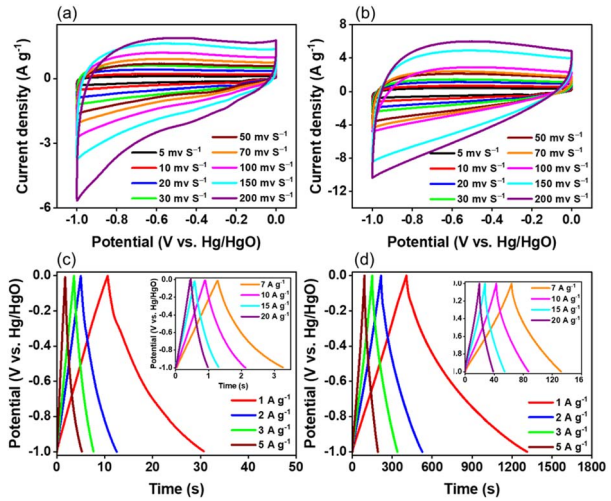

Fig. 8 CV profiles of (a) TAT-BCz CMP, and (b) TAT-BCz-800. The corresponding GCD profiles of (c) TAT-BCz CMP, and (d) TAT-BCz-800, recorded at various current densities in the three electrodes system.

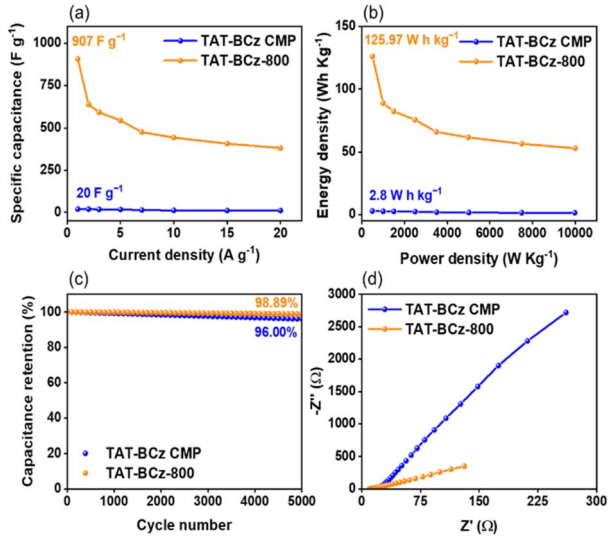

Fig. 9 (a) GCD specific capacitances of TAT-BCz CMP and TAT-BCz-800 recorded at current densities from 1.0 to 10 A g^{-1}. (b) Ragone plots. (c) Cycling retention of the electrodes, recorded at a current density of 10 A g^{-1} over 5000 cycles. (d) Nyquist plots of cells holding the as-synthesized materials in the three electrodes system.

with the subsequent steps of carbonization and KOH activation at higher temperatures, have been identified as crucial factors that enhance the electrochemical efficiency of the CMPs in SC applications.

According to Ragone plots, the energy density for TAT-Cz-800 and TAT-BCz-800 carbons were determined to be 139.58 and 125.97 W h kg^{-1}, respectively, while operating at a power density of 500 W kg^{-1}. These values significantly outperformed those of TAT-Cz CMP (2.39 W h kg^{-1}) and TAT-BCz polymer (2.8 W h kg^{-1}). In summary, the enhanced energy density values of the carbon materials were mainly due to their great surface area and exceptional conductivity (Fig. 7b and 9b). By comparison of the electrochemical analyses we obtained with those from previously reported efficient electrode materials, our prepared carbons have showcased themselves as some of the most dependable candidates for SCs applications.

We have also assessed the capacitance retention of our materials by subjecting them to 5000 GCD cycles at 10 A g^{-1} (Fig. 7c and 9c). Remarkably, the cyclic stability of the resulting microporous carbon materials, TAT-Cz-800 (98.59%) and TAT-BCz-800 (98.89%), surpassed those of their initial polymer counterparts, TAT-Cz CMP (97.5%) and TAT-BCz CMP (96%). These materials demonstrated outstanding cyclic stability even at higher current densities over extended cycling.

To gain a deeper understanding of ion transport behavior and internal resistance before and after carbonization, we conducted electrochemical impedance spectroscopy (EIS) and analyzed Nyquist plots for all polymers and their carbons (Fig. 7d and 9d). The EIS analyses of the carbonaceous materials displayed subtle arcs at elevated frequency, indicating resistive charge transfer (RCT) as well as mass transfer operations. The intersections of these semi-circles with the *x*-axis represent the equivalent series resistance (ESR), which comprises the contact resistance between the electrode and the current collector, besides the intrinsic resistance within the electrode material and the electrolyte.[80]

The significant surface areas of our synthesized carbon materials offer a substantial contact area for interaction between the electrodes and KOH ions, suggesting the existence of additional active positions for energy storage. The resultant carbons were featured by depressed values of ESR in agreement with their large surface areas. Furthermore, the presence of heteroatoms on the surface of electrodes enhanced wettability.[105] The Nyquist curves represented the resistance of TAT-Cz CMP, TAT-Cz-800, TAT-BCz CMP and TAT-BCz-800 to be 11.17, 10.38, 11.83, and 9.74 Ω, respectively, displaying lower resistance and delivering higher specific capacitance of our electrode materials.

The Bode curves of frequency-dependent resistance magnitude are depicted in Fig. S21.† The obtained plots for the triazatruxene-based polymers and their corresponding carbonaceous materials represented negative-sloped diagonal lines at lower frequencies and depressed values of ohmic resistance at elevated frequencies. This observation validates their advantageous electrochemical characteristics. In addition, the Bode patterns of the frequency-dependent phase angle have been investigated for all studied materials. (Fig. S22†) The determined knee frequencies at 45° phase angle for TAT-Cz CMP, TAT-Cz-800, TAT-BCz CMP and TAT-BCz-800 were 242.06, 2.86, 197.67 and 41.35 Hz, respectively. It was reported in literature that the rate efficacy for electrodes is directly related to the value of knee frequency, and hence, as the knee frequency value increases, the rate efficiency becomes better.[106] By studying the produced values of all materials, one can conclude that our polymers and their corresponding carbons possessed outstanding electrochemical efficiencies.

To gain a better understanding of the capacitive contribution of TAT-Cz-800 and TAT-BCz-800 carbon materials, we have examined the relationship between electrical current (i) and the scan rate potential (v) using the following power law equation.[107]

$$i = av^b \quad (1)$$

The slope of a log(i) *versus* log(v) plot was employed to estimate the value of "b", where "a" represents a constant value. The TAT-Cz-800 exhibited calculated b value of 0.97 and 0.81 for the anodic and cathodic peaks, respectively (Fig. 10a), while the TAT-BCz-800 exhibited calculated b value of 0.70 and 0.44 for the anodic and cathodic peaks, respectively (Fig. 10b).

These observations indicated the potential coexistence of capacitive and diffusion-controlled energy storage mechanisms for these two carbonaceous materials.[108] The superior rate capacity of TAT-Cz-800 is evidenced by its higher capacitive contribution compared to that of TAT-BCz-800. The capacitive contribution to overall capacity has been quantified by the utilizing of the following relation.[107]

$$i(V) = k_1 v + k_2 v^{1/2} \quad (2)$$

For a constant potential V, the total current is represented by $i(V)$, where $k_2 v^{1/2}$ and $k_1 v$ are the currents produced from the diffusion-controlled mechanism and capacitive effects, respectively. At 5 mV s^{-1}, the capacitive contributions of the TAT-Cz-800 and TAT-BCz-800 were estimated to be 78% and 21% of the total capacity, respectively. As the scan rate potential increased from 5 to 200 mV s^{-1}, the capacitive contribution raised to 96% for the TAT-Cz-800, and 63% for the TAT-BCz-800 (Fig. 10c and d).

To delve deeper into the practical application potential of TAT-based microporous carbons in SCs, the assembled symmetric coin SC has been investigated within a two-electrode system. The CV and GCD profiles have been measured across the potential range of 0.3 to −0.2 V. This was conducted at various sweep rates ranging from 10 to 200 mV s^{-1} and current densities spanning from 1.0 to 20 A g^{-1} (Fig. 11). As depicted in Fig. 11a and b, the CVs maintain a rectangular shape across various scan rates, even at a high rate of 200 mV s^{-1}. This behavior was observed particularly for the TAT-Cz-800 carbons which indicates an EDLC manner. In addition, with the escalating scan rate, there's a concurrent rise in the current observed at the identical potential, signifying the excellent reversibility of the symmetric capacitor. Furthermore, the GCD profiles of the carbon-based symmetric cell exhibit a triangular shape, suggesting robust capacitance efficiency (Fig. 11c and d). Notably, the electrochemical capacitance of the TAT-Cz-800 had an impressive value of 458 F g^{-1} at 1.0 A g^{-1} surpassing the capacitance of the TAT-BCz-800 (287 F g^{-1}), aligning well with the outcomes from the three-electrode experiments (Fig. 12a).

As evident, the two-electrode coin system yields different specific capacitance values compared to the three-electrode

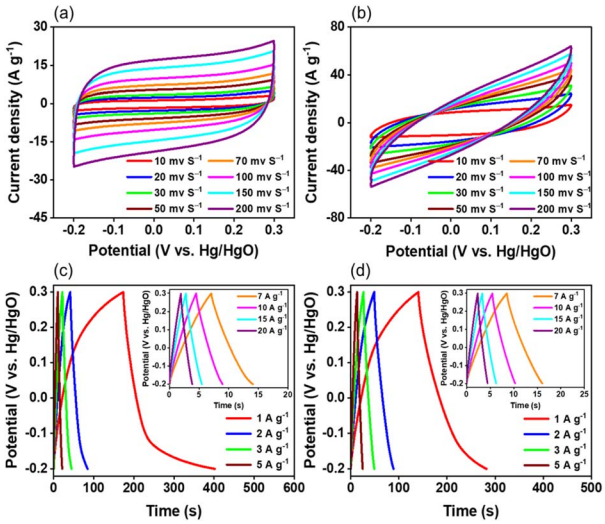

Fig. 11 CV profiles of (a) TAT-Cz-800, and (b) TAT-BCz-800. The corresponding GCD profiles of (c) TAT-Cz-800, and (d) TAT-BCz-800, recorded at various current densities in the two electrodes system.

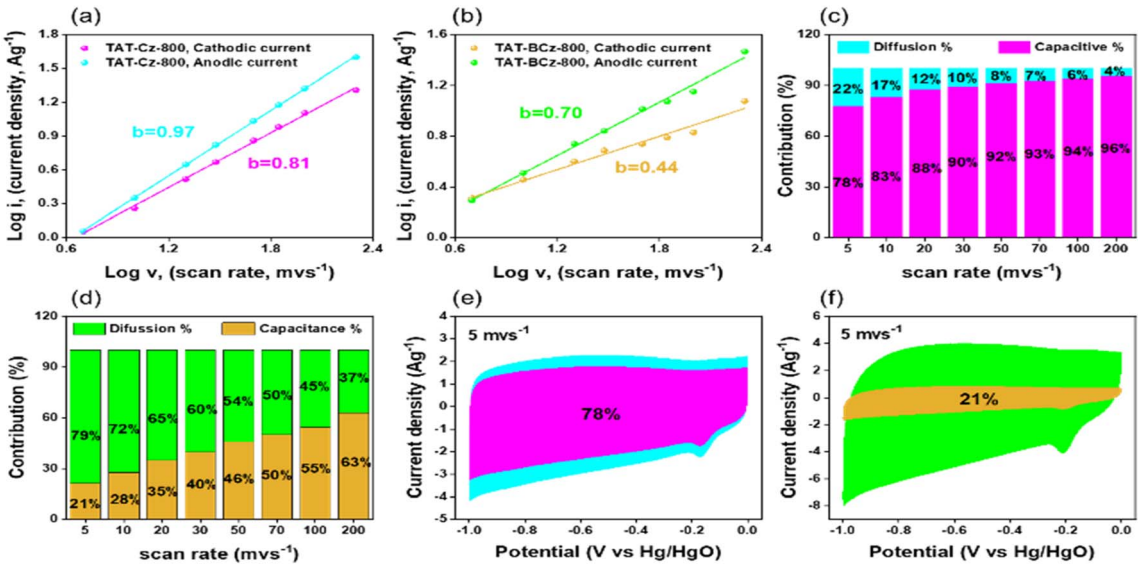

Fig. 10 (a and b) Log(i) *versus* log(v) plots of (a) TAT-Cz-800, and (b) TAT-BCz-800 carbons. (c and d) The relative contribution of the capacitive and diffusion-controlled energy storage of (c) TAT-Cz-800, and (d) TAT-BCz-800 carbons, recorded at various scan rates. (e and f) The relative contributions of capacitive and diffusion currents of (e) TAT-Cz-800, and (f) TAT-BCz-800 carbons, recorded at 5 mV s^{-1}.

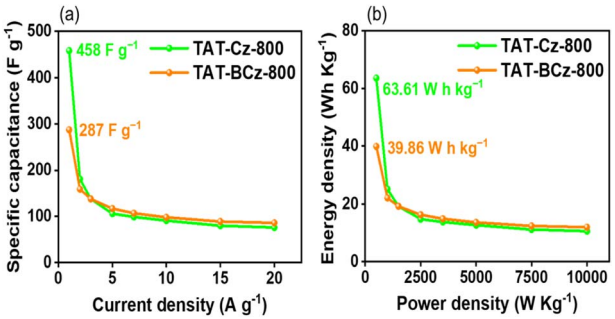

Fig. 12 (a) GCD specific capacitances of TAT-Cz-800 and TAT-BCz-800 recorded at current densities from 1.0 to 20 A g^{-1}. (b) Ragone plots in the two electrodes system.

system. In the three-electrode system, the obtained electrochemical capacitance value is typically four times higher than that for the two-electrode coin system. This disparity arises because the coin system includes double-layer loading at both electrodes, akin to having two capacitors in series, in comparable to the three-electrode system which has only one double layer. Hence, the specific capacitance resulted from the coin system is often known as the device capacitance (C_{device}), whereas the specific capacitance of the three-electrode system is referred as the material capacitance ($C_{material}$), which correlated by the following equation:[109]

$$C_{material} = 4C_{device} \quad (3)$$

The Ragone plot, illustrating the performance of the TAT-based symmetric cell, has been represented in Fig. 12b. Notably, the TAT-Cz-800 electrode showed an impressive energy density of 63.61 W h kg^{-1} at a power density of 500 W kg^{-1}. Even at an escalated power density of 10 000 W kg^{-1}, it maintained an energy density of 10.56 W h kg^{-1}, which was greater than those of the TAT-BCz-800 electrode and previously reported materials. In addition, Fig. S23† displayed the Nyquist plots of TAT-Cz-800 and TAT-BCz-800 electrode materials. At high-frequency values, all samples demonstrate a distinct semicircular feature, representing the R_{ct}. Remarkably, the TAT-BCz-800 demonstrated the smallest R_{ct} (2.16 Ω) in comparison to the TAT-Cz-800 (1.65 Ω), implying the least resistance for electron charge transfer within the electrode.

Moreover, the Bode plots were utilized to estimate both the resistance characteristics and the knee frequencies for the synthesized carbon materials. As shown in Fig. S24,† these carbon-based electrodes represented negative slopes' lines at lower frequencies, and minimal ohmic resistance at elevated frequencies, and the calculated knee frequencies at 45° phase angle were 11.18 and 41.75 Hz, for TAT-Cz-800 and TAT-BCz-800, respectively.

Conclusions

In this study, an easy synthetic approach was employed to construct nitrogen-rich triazatruxene-based CMPs and their corresponding carbonized forms at elevated temperature. The characterization encompassing BET, TGA, SEM, and TEM revealed that the produced carbon materials exhibited exceptional attributes, including high specific surface area (up to 600 m^2 g^{-1}), remarkable thermal stability (T_{d10} of 791 °C and a char yield of 90%), and a microporous carbon structure. Furthermore, the optimized porous carbon material known as TAT-Cz-800 displayed impressive traits in terms of redox efficiency, electrical conductivity, and physical robustness. Consequently, its electrode material manifested a peak electrochemical capacitance of 1005 F g^{-1} at a current density of 1.0 A g^{-1}. Notably, this efficacy remained stable, with a retention stability of 98.59% after undergoing 5000 cycles at 10 A g^{-1}. Furthermore, a two-electrode SC holding TAT-Cz-800 displayed a prime capacitance (458 F g^{-1}) at 1.0 A g^{-1}, and an outstanding energy density (63.61 W h kg^{-1}). These findings validate the efficacy of employing carbonization and KOH activation of polymeric organic materials as a viable tactic for high performance SCs and offer valuable insights for the design of various electrodes for energy storage applications.

Conflicts of interest

There are no conflicts to declare.

Acknowledgements

This study was supported financially by the National Science and Technology Council, Taiwan, under contract 112-2221-E-110-005-MY3.

Notes and references

1 Y. Z. Zhang, Y. Wang, T. Cheng, L. Q. Yao, X. Li, W. Y. Lai and W. Huang, *Chem. Soc. Rev.*, 2019, **48**, 3229–3264.
2 F. Wang, X. Wu, X. Yuan, Z. Liu, Y. Zhang, L. Fu, Y. Zhu, Q. Zhou, Y. Wu and W. Huang, *Chem. Soc. Rev.*, 2017, **46**, 6816–6854.
3 W. Zhao, M. Jiang, W. Wang, S. Liu, W. Huang and Q. Zhao, *Adv. Funct. Mater.*, 2021, **31**, 2009136.
4 T. Cheng, Y. Z. Zhang, S. Wang, Y. L. Chen, S. Y. Gao, F. Wang, W. Y. Lai and W. Huang, *Adv. Funct. Mater.*, 2021, **31**, 2101303.
5 Y. Zhou, H. Qi, J. Yang, Z. Bo, F. Huang, M. S. Islam, X. Lu, L. Dai, R. Amal, C. H. Wang and Z. Han, *Energy Environ. Sci.*, 2021, **14**, 1854–1896.
6 D. Zhao, K. Jiang, J. Li, X. Zhu, C. Ke, S. Han, E. Kymakis and X. Zhuang, *BMC Mater.*, 2020, **2**, 3.
7 K. Jiang, I. A. Baburin, P. Han, C. Yang, X. Fu, Y. Yao, J. Li, E. Cánovas, G. Seifert and J. Chen, *Adv. Funct. Mater.*, 2020, **30**, 1908243.
8 H. F. An, Y. Wang, X. Y. Wang, N. Li and L. P. Zheng, *J. Solid State Electrochem.*, 2010, **14**, 651–657.
9 J. S. M. Lee and A. I. Cooper, *Chem. Rev.*, 2020, **120**, 2171–2214.
10 W. Lyu, W. Zhang, H. Liu, Y. Liu, H. Zuo, C. Yan, C. F. J. Faul, A. Thomas, M. Zhu and Y. Liao, *Chem. Mater.*, 2020, **32**, 8276–8285.
11 K. Amin, N. Ashraf, L. Mao, C. F. J. Faul and Z. Wei, *Nano Energy*, 2021, **85**, 105958.

12 A. F. M. EL-Mahdy, J. Lüder, M. G. Kotp and S. W. Kuo, *Polymers*, 2021, **13**, 1385.
13 T. L. Yang, J. Y. Chen, S. W. Kuo, C. T. Lo and A. F. M. El-Mahdy, *Polymers*, 2022, **14**, 3428.
14 M. Gao, M. J. Zheng, A. F. M. EL-Mahdy, C. W. Chang, Y. C. Su, W. H. Hung, S. W. Kuo and L. H. Yeh, *Nano Energy*, 2023, **105**, 108007.
15 L. R. Ahmed, L. Gilmanova, C. T. Pan, S. Kaskel and A. F. M. EL-Mahdy, *ACS Appl. Polym. Mater.*, 2022, **4**, 9132–9143.
16 Y. Kou, Y. Xu, Z. Guo and D. Jiang, *Angew. Chem., Int. Ed.*, 2011, **123**, 8912–8918.
17 M. Xu, S. Zhang, T. Wang, B. Yu, Z. Yang, X. Wang, R. Zhou and D. Hua, *ACS Appl. Mater. Interfaces*, 2022, **14**, 7826–7835.
18 A. Thomas, P. Kuhn, J. Weber, M. M. Titirici and M. Antonietti, *Macromol. Rapid Commun.*, 2009, **30**, 221–236.
19 J. X. Jiang, C. Wang, A. Laybourn, T. Hasell, R. Clowes, Y. Z. Khimyak, J. Xiao, S. J. Higgins, D. J. Adams and A. I. Cooper, *Angew. Chem., Int. Ed.*, 2011, **50**, 1072–1077.
20 J. H. Wang, C. L. Chang, Z. W. Zhang and A. F. M. EL-Mahdy, *Polym. Chem.*, 2022, **13**, 5300–5308.
21 Z. Zhu, Z. Yan, Y. Fan, C. Liu, H. Sun, W. Liang and A. Li, *ACS Appl. Energy Mater.*, 2020, **3**, 5260–5268.
22 L. Shu, J. Yu, Y. Cui, Y. Ma, Y. Li, B. Gao and H. G. Wang, *Int. J. Hydrogen Energy*, 2022, **47**, 10902–10910.
23 Z. Xie, C. Wang, K. E. DeKrafft and W. Lin, *J. Am. Chem. Soc.*, 2011, **133**, 2056–2059.
24 P. Ju, W. Qi, B. Guo, W. Liu, Q. Wu and Q. Su, *Catal. Lett.*, 2022, **153**, 2125–2136.
25 L. Ren and T. Geng, *Bull. Mater. Sci.*, 2022, **45**, 137.
26 C. G. Bezzu, M. Carta, A. Tonkins, J. C. Jansen, P. Bernardo, F. Bazzarelli and N. B. McKeown, *Adv. Mater.*, 2012, **24**, 5930–5933.
27 Z. Wei, D. Wang, Y. Liu, X. Guo, Y. Zhu, Z. Meng, Y. ZQ and W. Y. Wong, *J. Mater. Chem. C*, 2020, **8**, 10774–10780.
28 L. R. Ahmed, C. H. Chuang, J. Lüder, H. W. Yang and A. F. M. EL-Mahdy, *Macromolecules*, 2022, **55**, 10197–10209.
29 Y. Liao, H. Wang, M. Zhu and A. Thomas, *Adv. Mater.*, 2018, **30**, 1705710.
30 W. Zhang, H. Zuo, Z. Cheng, Y. Shi, Z. Guo, N. Meng, A. Thomas and Y. Liao, *Adv. Mater.*, 2022, **34**, 2104952.
31 H. Li, W. Lyu and Y. Liao, *Macromol. Rapid Commun.*, 2019, **40**, 1900455.
32 Y. Li, G. Wang, T. Wei, Z. Fan and P. Yan, *Nano Energy*, 2016, **19**, 165–175.
33 T. A. Gaber, L. R. Ahmed and A. F. M. EL-Mahdy, *J. Mater. Chem. A*, 2023, **11**, 19408–19417.
34 J. Zhan and A. F. M. EL-Mahdy, *Chem. Eng. J.*, 2023, **473**, 145124.
35 K. Y. Lin and A. F. M. EL-Mahdy, *Mater. Chem. Phys.*, 2022, **281**, 125850.
36 A. Khan, R. A. Senthil, J. Pan, S. Osman, Y. Sun and X. Shu, *Electrochim. Acta*, 2020, **335**, 135588.
37 H. Wang, Z. Cheng, Y. Liao, J. Li, J. Weber, A. Thomas and C. F. J. Faul, *Chem. Mater.*, 2017, **29**, 4885–4893.
38 L. R. Ahmed, A. F. M. EL-Mahdy, C. T. Pan and S. W. Kuo, *Mater. Adv.*, 2021, **2**, 4617–4629.
39 M. A. Shannon, P. W. Bohn, M. Elimelech, J. G. Georgiadis, B. J. Marinas and A. M. Mayes, *Nature*, 2008, **452**, 301–310.
40 H. W. Kim, H. W. Yoon, S. M. Yoon, B. M. Yoo, B. K. Ahn, Y. H. Cho, H. J. Shin, H. Yang, U. Paik, S. Kwon, J. Y. Choi and H. B. Park, *Science*, 2013, **342**, 91–95.
41 H. Li, J. Li, A. Thomas and Y. Liao, *Adv. Funct. Mater.*, 2019, **29**, 1904785.
42 S. Liu, J. Yang, M. Wang, X. Che, Y. Liu and J. Qiu, *ACS Appl. Energy Mater.*, 2023, **6**, 2989–2998.
43 X. G. Che, J. Jin, Y. X. Zhang, S. Y. Liu, M. Wang and J. Yang, *New Carbon Mater.*, 2023, **38**, 1050–1058.
44 M. Wang, J. Yang, S. Liu, X. Che, S. He, G. Chen and J. Qiu, *J. Chem. Eng.*, 2023, **451**, 138501.
45 F. Rodríguez-Reinoso and M. Molina-Sabio, *Carbon*, 1992, **30**, 1111.
46 J. Wang and S. Kaskel, *J. Mater. Chem.*, 2012, **22**, 23710.
47 Y. Zhu, S. Murali, M. D. Stoller, K. J. Ganesh, W. Cai, P. J. Ferreira, A. Pirkle, R. M. Wallace, K. A. Cychosz, M. Thommes, D. Su, E. A. Stach and R. S. Ruoff, *Science*, 2011, **332**, 1537.
48 D. Liu, W. Zhang, H. Lin, Y. Li, H. Lu and Y. Wang, *J. Cleaner Prod.*, 2016, **112**, 1190.
49 M. M. Samy, M. G. Mohamed and S. W. Kuo, *Eur. Polym. J.*, 2020, **138**, 109954.
50 M. G. Mohamed, M. M. M. Ahmed, W. T. Du and S. W. Kuo, *Molecules*, 2021, **26**, 738.
51 A. F. Saber, M. Ahmed, S. W. Kuo and A. F. M. EL-Mahdy, *Polym. Chem.*, 2023, **14**, 4079–4088.
52 E. M. García-Frutos, C. Coya, E. Gutierrez, A. Monge, A. de Andrés and B. Gómez-Lor, *Proc. of SPIE Org.*, 2010, **7778**, 777806.
53 X. C. Li, C. Y. Wang, W. Y. Lai and W. Huangab, *J. Mater. Chem. C*, 2016, **4**, 10574–10587.
54 J. H. Kim, K. H. Lee and J. Y. Lee, *J. Mater. Chem. C*, 2020, **8**, 5265–5272.
55 Y. Zhou, Y. Li, S. Wua, Y. Zhao, T. Yu, W. Su, H. Ma, L. Qian and R. Wang, *Dyes Pigm.*, 2021, **188**, 109165.
56 I. Bulut, P. Chávez, A. Mirloup, Q. Huaulmé, A. Hébraud, B. Heinrich, S. Fall, S. Méry, R. Ziessel, T. Heiser, P. Léveque and N. Leclerc, *J. Mater. Chem. C*, 2016, **4**, 4296–4303.
57 C. Ruiz, I. Arrechea-Marcos, A. Benito-Hernández, E. Gutierrez-Puebla, M. A. Monge, J. T. López Navarrete, M. C. Ruiz Delgado, R. Ponce Ortiz and B. Gómez-Lor, *J. Mater. Chem. C*, 2018, **6**, 50–56.
58 Y. Zheng, N. A. Khan, X. Ni, K. A. I. Zhang, Y. Shen, N. Huang, X. Y. Kong and L. Ye, *Chem. Commun.*, 2023, **59**, 6314–6334.
59 Y. Wang, S. Sun, X. Wu, H. Liang and W. Zhang, *Nano-Micro Lett.*, 2023, **15**, 78.
60 X. Gao, Z. Xiao, L. Jiang, C. Wang, X. Lin and L. Sheng, *J. Colloid Interface Sci.*, 2023, **641**, 820–830.
61 A. F. Saber, A. M. Elewa, H. H. Chou and A. F. M. EL-Mahdy, *Appl. Catal., B*, 2022, **316**, 121624.

62 C. L. Chang, A. M. Elewa, J. H. Wang, H. H. Chou and A. F. M. EL-Mahdy, *Microporous Mesoporous Mater.*, 2022, **345**, 112258.
63 T. Techajaroonjit, S. Namuangruk, N. Prachumrak, V. Promarak, M. Sukwattanasinitt and P. Rashatasakhon, *RSC Adv.*, 2016, **6**, 56392.
64 S. Zang, J. Jiang, Y. An, Z. Li, H. Guo, Y. Sun, H. Dou and X. Zhang, *J. Electroanal. Chem.*, 2020, **876**, 114723.
65 Y. Zhang, F. Deng, Q. Zhang, B. Xing, J. Shang and J. Lin, *J. Energy Storage*, 2022, **55**, 105494.
66 G. Li, Y. Li, X. Chen, X. Hou, H. Lin and L. Jia, *J. Colloid Interface Sci.*, 2022, **605**, 71–81.
67 N. Wang, Y. Yao, L. He, Y. Chen and B. Sun, *J. Porous. Mater.*, 2020, **27**, 627–635.
68 Y. Liu, Z. Xiao, Y. Liu and L. Z. Fan, *J. Mater. Chem. A*, 2018, **6**, 160–166.
69 K. Zou, Y. Deng, J. Chen, Y. Qian, Y. Yang, Y. Li and G. Chen, *J. Power Sources*, 2018, **378**, 579–588.
70 J. Wang, F. Qin, Z. Guo and W. Shen, *ACS Sustain. Chem. Eng.*, 2019, **7**, 11550–11563.
71 X. Wang, M. Lou, X. Yuan, W. Dong, C. Dong, H. Bi and F. Huang, *Carbon*, 2017, **118**, 511–516.
72 B. Tan, H. Luo and Z. Xie, *Chemistry Select*, 2018, **3**, 6440–6449.
73 E. Frackowiak and F. Beguin, *Carbon*, 2001, **39**, 937–950.
74 E. Frackowiak, *Phys. Chem. Chem. Phys.*, 2007, **9**, 1774–1785.
75 X. Zhao, Y. Zhou, Y. L. Xu, C. Huang, Y. P. Shen, Y. Zhang, Z. F. Fan, Q. L. Tang, A. P. Hu and X. H. Chen, *J. Storage Mater.*, 2022, **52**, 104642.
76 Y. Fang, B. Luo, Y. Jia, X. Li, B. Wang, Q. Song, F. Kang and L. Zhi, *Adv. Mater.*, 2012, **24**, 6348–6355.
77 M. G. Mohamed, M. Y. Tsai, W. C. Su, A. F. M. EL Mahdy, C. F. Wang, C. F. Huang, L. Dai, T. Chen and S. W. Kuo, *Mater. Today Commun.*, 2020, **24**, 101111.
78 X. Xu, K. Sielicki, J. Min, J. Li, C. Hao, X. Wen, X. Chen and E. Mijowska, *Renewable Energy*, 2022, **185**, 187–195.
79 Y. Zhu, Z. Li, Y. Tao, J. Zhou and H. Zhang, *J. Energy Storage*, 2022, **47**, 103624.
80 G. Li, Y. Li, X. Chen, X. Hou, H. Lin and L. Jia, *J. Colloid Interface Sci.*, 2022, **605**, 71–81.
81 N. B. Gday, S. Altın, S. Yasar and Y. Altın, *Int. J. Energy Res.*, 2022, **46**, 795–809.
82 J. Wang, P. Zhang, L. Liu, Y. Zhang, J. Yang, Z. Zeng and S. Deng, *Chem. Eng. J.*, 2018, **348**, 57–66.
83 Y. Zhao, N. Bu, H. Shao, Q. Zhang, B. Feng, Y. Xu, G. Zheng, Y. Yuan, Z. Yan and L. Xia, *New J. Chem.*, 2019, **43**, 18158–18164.
84 N. Deka, R. Patidar, S. Kasthuri, N. Venkatramaiah and G. K. Dutta, *Mater. Chem. Front.*, 2019, **3**, 680–689.
85 G. Huang, Q. Geng, B. Xing, Y. Liu, Y. Li, Q. Liu, J. Jia, L. Chen and C. Zhang, *J. Power Sources*, 2020, **449**, 227506.
86 T. Periyasamy, S. P. Asrafali and S. C. Kim, *Polymers*, 2023, **15**, 1564.
87 W. Wang, W. Liu, Y. Zeng, Y. Han, M. Yu, X. Lu and Y. Tong, *Adv. Mater.*, 2015, **27**, 3572–3578.
88 C. Su, H. He, L. Xu, K. Zhao, C. Zheng and C. Zhang, *J. Mater. Chem. A*, 2017, **5**, 2701–2709.
89 A. M. Khattak, Z. A. Ghazi, B. Liang, N. A. Khan, A. Iqbal, L. Li and Z. A. Tang, *J. Mater. Chem. A*, 2016, **4**, 16312–16317.
90 C. Sengottaiyan, R. Jayavel, R. G. Shrestha, T. Subramani, S. Maji, J. H. Kim, J. P. Hill, K. Ariga and L. K. Shrestha, *Bull. Chem. Soc. Jpn.*, 2019, **92**, 521–528.
91 A. H. Khan, S. Ghosh, B. Pradhan, A. Dalui, L. K. Shrestha, S. Acharya and K. Ariga, *Bull. Chem. Soc. Jpn.*, 2017, **90**, 627–648.
92 J. Yan, Q. Wang, T. Wei and Z. Fan, *Adv. Energy Mater.*, 2014, **4**, 1300816.
93 F. Su, C. K. Poh, J. S. Chen, G. Xu, D. Wang, Q. Li, J. Lin and X. W. Lou, *Energy Environ. Sci.*, 2011, **4**, 717.
94 L. Sheng, L. Jiang, T. Wei, Z. Liu and Z. Fan, *Adv. Energy Mater.*, 2017, **7**, 1700668.
95 A. Vervald, K. Kozhushnyi and T. Dolenko, *Carbon Nanostruct.*, 2022, **30**, 106–112.
96 L. Wang, X. Li, R. Liu, Y. Wang, Y. Bai, Y. Liu, Y. Ma, G. Yuan and Z. Guo, *Nano Energy*, 2021, **80**, 105572.
97 Y. Zhang and P. T. Cummings, *ACS Appl. Mater. Interfaces*, 2019, **11**, 42680–42689.
98 B. Zahiri, R. M. Felix, A. Hill, C. H. Kung, T. Sharma, J. D. Real and W. Mérida, *Appl. Surf. Sci.*, 2018, **458**, 32–42.
99 J. Lee and G. H. An, *Appl. Surf. Sci.*, 2021, **539**, 148290.
100 Y. Zhang, Y. Cong, J. Zhang, X. Li, Y. Li, Z. Dong, G. Yuan, J. Zhang and Z. Cui, *Surf. Coat. Technol.*, 2018, **349**, 384–391.
101 J. Song, W. Li, J. Xin, W. Wang, K. Song, X. Chen and G. Yin, *Appl. Surf. Sci.*, 2021, **568**, 150915.
102 M. Mirzaeian, A. A. Ogwu, H. F. Jirandehi, S. Aidarova, Z. Ospanova and N. Tsendzughul, *Colloids Surf., A*, 2017, **519**, 223–230.
103 M. Li, H. Niu, K. Shang, Y. Gao, B. Li, L. Jiang, Z. Zhao, X. Li, S. Wang and Y. Feng, *J. Langmuir.*, 2022, **38**, 15353–15360.
104 J. Liu, D. Xuan, Z. Lu, Z. Wang, Q. Liu, S. Li, D. Wang, Y. Ye, D. Wang and Z. Zheng, *Appl. Surf. Sci.*, 2022, **573**, 151626.
105 Y. Shu, Q. Bai, G. Fu, Q. Xiong, C. Li, H. Ding, Y. Shen and H. Uyama, *Carbohydr. Polym.*, 2020, **227**, 115346–115358.
106 W. Lyu, C. Yan, Z. Chen, J. Chen, H. Zuo, L. Teng, H. Liu, L. Wang and Y. Liao, *ACS Appl. Energy Mater.*, 2022, **5**, 3706–3714.
107 Q. Li, W. Lu, Z. Li, J. Ning, Y. Zhong and Y. Hu, *Chem. Eng. J.*, 2020, **380**, 122544.
108 E. Lim, C. Jo, H. Kim, M. H. Kim, Y. Mun, J. Chun, Y. Ye, J. Hwang, K. S. Ha, K. C. Roh, K. Kang, S. Yoon and J. Lee, *ACS Nano*, 2015, **9**, 7497–7505.
109 M. F. El-Kady and R. B. Kaner, *Nat. Commun.*, 2013, **4**, 1475.